JGR Atmospheres

RESEARCH ARTICLE
10.1029/2022JD037795

Key Points:

- Subseasonal monsoon variability is linked to rainfall signals over U.S. Great Plains and its associated dynamical drivers
- A cause-and-effect algorithm verified a pathway from regional monsoon rainfall to Great Plains rainfall, which takes approximately 2 weeks
- Weekly East Asian monsoon rainfall is causally linked to Rossby wave excitation and active Great Plains convection about 1 week later

Correspondence to:
K. Malloy,
kmm2374@columbia.edu

Citation:
Malloy, K., & Kirtman, B. P. (2023). Subseasonal Great Plains rainfall via remote extratropical teleconnections: Regional application of theory-guided causal networks. *Journal of Geophysical Research: Atmospheres*, *128*, e2022JD037795. https://doi.org/10.1029/2022JD037795

Received 6 SEP 2022
Accepted 14 FEB 2023

Author Contributions:
Conceptualization: Kelsey Malloy
Formal analysis: Kelsey Malloy
Funding acquisition: Ben P. Kirtman
Investigation: Ben P. Kirtman
Methodology: Kelsey Malloy
Supervision: Ben P. Kirtman
Visualization: Kelsey Malloy
Writing – original draft: Kelsey Malloy
Writing – review & editing: Ben P. Kirtman

Subseasonal Great Plains Rainfall via Remote Extratropical Teleconnections: Regional Application of Theory-Guided Causal Networks

Kelsey Malloy[1] **and Ben P. Kirtman**[2]

[1]Department of Applied Physics and Applied Mathematics, Columbia University, New York, NY, USA, [2]Rosenstiel School of Marine and Atmospheric Science, University of Miami, Miami, FL, USA

Abstract Long-range U.S. summer rainfall prediction skill is low. Monsoon variability, especially over the West North Pacific Monsoon (WNPM) and/or East Asian Monsoon (EAM) region, can influence U.S. Great Plains hydroclimate variability via a forced Rossby wave response. Here, we explored subseasonal monsoon variability as a source of predictability for Great Plains rainfall. The boreal summer intraseasonal oscillation (BSISO) is related to Great Plains convection and Great Plains low-level jet (LLJ) anomalies as well as a cross-Pacific wave train. Using a causal effect network, we found that the time between BSISO-related geopotential height anomalies and Great Plains rainfall anomalies is about 2 weeks; therefore, BSISO convection may be a valuable forecast of opportunity for subseasonal prediction of Great Plains convection anomalies. More specifically, causal link patterns/maps revealed that the above-normal weekly EAM rainfall, rather than WNPM rainfall or general geopotential height activity over the East Asia, was causally linked to Great Plains LLJ strengthening and active Great Plains convection the following week.

Plain Language Summary Forecasting U.S. summer rainfall out past ~7–10 days, considered the subseasonal timescale, is a challenge. However, there are times when subseasonal forecast skill is relatively higher due to propagating atmospheric waves from remote climate events. The West North Pacific Monsoon (WNPM) and East Asian Monsoon (EAM) can provide a remote influence via their related heating triggering atmospheric waves. Using an algorithm that effectively identifies and quantifies cause-and-effect relationships, we constructed a network that connects EAM rainfall and Great Plains rainfall via these atmospheric waves. We found that above-normal EAM rainfall, rather than WNPM rainfall or general atmospheric wave activity over the East Asia, was causally linked to active Great Plains convection the following week. Therefore, monsoon variability, especially over the EAM region, might be a valuable source of subseasonal predictability for U.S. summer rainfall.

1. Introduction

Understanding summertime continental U.S. (CONUS) hydroclimate predictability on the subseasonal-to-seasonal (S2S) timescale has been challenging, and relationships between tropical remote forcing and mid-latitude circulation are difficult to assess due to the overall weak signals of the summer season (Trenberth et al., 1998; S. Zhou et al., 2012). Many studies suggest that Asian summer monsoon (ASM) variability on the seasonal-to-interannual timescale, especially over the West North Pacific (WNPM) and/or East Asian Monsoon (EAM) region, can influence CONUS hydroclimate via a quasi-stationary Rossby wave response (Di Capua et al., 2020b; Kornhuber et al., 2019; Lopez et al., 2019; Malloy & Kirtman, 2022; Yang et al., 2020; Zhu & Li, 2016, 2018). The Great Plains low-level jet (LLJ) is the prominent transporter of moisture into that region, and large-scale LLJ anomalies are typically associated with rainfall events (Algarra et al., 2019; Arritt et al., 1997; Cook et al., 2008; Higgins et al., 1997; Malloy & Kirtman, 2020; Nayak & Villarini, 2017; Weaver & Nigam, 2008; Weaver et al., 2009). The upper-level pattern associated with the monsoon-forced Rossby wave response can often align (constructively interfere) with the Great Plains LLJ to amplify Great Plains rainfall signals (Agrawal et al., 2021).

The ASM also exhibits subseasonal variability, typically called the boreal summer intraseasonal oscillation (BSISO), and it is the dominating mode of tropical convection over ASM region and western Pacific (S. S. Lee & Wang, 2016; Yasunari, 1979, 1980). Krishnamurthy et al. (2021) and Moon et al. (2013) identified the monsoon intraseasonal oscillation as a source of subseasonal predictability over CONUS in the summer in observations and/or climate forecast models. Few studies have explored the dynamical pathway between BSISO-related

anomalies and Great Plains rainfall anomalies, such as understanding the timescale of Rossby wave initiation and propagation to influence North American features, such as the Great Plains LLJ.

In many of these studies, climate models were used to quantify the monsoon responses, usually by prescribed heating, and were compared to observations (Lopez et al., 2019; Malloy & Kirtman, 2022; Yang et al., 2020). In this case, causality is implied (amongst natural variability or chaos). For example, the EAM heating causes the elongated anomalous ridge over the North Pacific, anomalous trough over western North America, and anomalous ridge over eastern North America from the set of experiments in Malloy and Kirtman (2022). However, there are also ways to quantify causal links via data-driven methods that is, using observations alone. Causal discovery methods, such as causal effect networks (CENs), are becoming popular as a way to map physical links in the climate system within an inputted timeseries of data (Kretschmer et al., 2016; Runge, 2018, 2020; Runge et al., 2014, 2019). Using CENs, Di Capua et al. (2020a) found that there was a link between the North Atlantic Oscillation (NAO), circumglobal teleconnection (CGT), and ASM variability, as well as between the BSISO and ASM variability. Di Capua et al. (2020b) suggested that the WNPM may force the North Pacific circulation which subsequently influences temperature and rainfall anomalies over North America.

The CENs methodology is an application of the Peter and Clark Momentary Conditional Independence (PC-MCI) algorithm (Runge et al., 2019, 2014; Spirtes et al., 2000), used to effectively determine causal links while removing the effects from autocorrelation, indirect (spurious) links, or common drivers. It maintains a high detection power over other techniques, such as Granger causality model (Runge, 2018, 2020; Runge et al., 2019). There are many assumptions in using CENs, including that causality can only be determined among the given drivers. Adding or removing drivers can change the conditional (in)dependence and hence change the linkages. Therefore, knowledge of the physical system beforehand, including relevant variables and timescales, is essential for interpreting the output of the algorithm.

The objective of this study is to: (a) identify potential remote drivers of U.S. rainfall variability, and (b) apply a theory-guided CEN approach to analyze the causality and pathway between these remote drivers and Great Plains LLJ and rainfall anomalies on the subseasonal timescale. This extends upon the methodology from Di Capua et al. (2020a) and Di Capua et al. (2020b) by applying it to understand more regional-scale monsoon forcing mechanisms. We also successfully isolate the impacts from interrelated drivers in the CEN with causal maps, shedding light on a source of U.S. Great Plains hydroclimate predictability.

2. Data and Methods

2.1. Observational Data Sets

This study focuses on the extended summer season (May through September), though April was considered for the lead-lag correlation analysis and CEN. Pressure-level meridional wind, zonal wind, geopotential height were taken from the European Center for Medium-Range Weather Forecasts fifth-generation reanalysis (ERA5). ERA5 atmospheric data is provided hourly on a 0.25° latitude/longitude grid (Hersbach et al., 2020), and it is recalculated to daily averages. U.S. precipitation data were taken from the Climate Prediction Center (CPC) Global Unified Gauge-based Analysis, provided on a 0.5° latitude/longitude grid over land (Chen et al., 2008; Xie et al., 2007). Outgoing Longwave Radiation (OLR) data, used as a proxy for convection, were taken from the interpolated daily OLR version 1.2 from National Oceanic and Atmospheric Administration Climate Data Record, accessed from https://www.ncei.noaa.gov/access/metadata/landing-page/bin/iso?id=gov.noaa.ncdc:C00875.

Because this study is focused on intraseasonal variability, for every variable, we removed the centered 120-day moving mean at every grid point (Arcodia et al., 2020) in addition to detrending and removing the annual cycle. Then we took the centered 10-day running mean of the variables to focus on large-scale, low-frequency features. This filtering step is done to focus on variability between synoptic and seasonal timescales. For the CEN analysis, we used the filtered data and resampled the data as weekly averages; using weekly data is a practical approach for subseasonal predictability analysis in order to filter short-term temporal fluctuations and simplify the visualized CEN (Di Capua et al., 2020a; Di Capua et al., 2020b; Krishnamurthy et al., 2021).

2.2. Potential Drivers

The Great Plains precipitation index is defined by averaged precipitation anomalies within the 35°–50°N, 85°–105°W domain, and the Great Plains LLJ index is defined by the averaged V850 anomalies within the

Table 1
Potential Drivers to Great Plains Rainfall

Name	Identifier	Index calculation
Great Plains precipitation	*GP rainfall*	*Precipitation*[35°–50°N, 85°–105°W]*
Great Plains low-level jet	GPLLJ	V850*[25°–35°N, 90°–102°W]
Pacific-North America High-Low dipole	PNA-HL	(Z200*[35°–60°N, 135°–165°W] − Z200*[35°–60°N, 100°–130°W])
North Pacific Low	NPac-L	Z200*[35°–60°N, 160°E−170°W]
East Asian Monsoon Low	EAM-L	Z200*[25°–50°N, 90°–130°E]
East Asian Monsoon precipitation	EAM rainfall	Precipitation*[20°–30°N, 100°–125°E]
West North Pacific Monsoon precipitation	WNPM rainfall	Precipitation*[0°–20°N, 90°–120°E]

Note. The Great Plains precipitation index (italicized) included here as predictand. Index is calculated by taking the domain-averaged anomalies of the variable.

25°–35°N, 90°–102°W domain. These domains are slightly larger than in previous literature (Malloy & Kirtman, 2020; Weaver & Nigam, 2008) to account for shifts eastward, which may be more important for EAM-forced Great Plains LLJ variability that is coupled to the upper levels (Agrawal et al., 2021). In addition, we defined various other indices to input into the CEN as potential drivers based on the lagged correlation analysis. All inputs, or potential drivers, to the Great Plains LLJ and Great Plains rainfall are outlined in Table 1 and can be visualized in the lagged correlation figures in Results section.

2.3. CENs

The CEN is constructed by first applying the PC-MCI algorithm (Runge et al., 2014, 2019; Spirtes et al., 2000). This is a two-step procedure: (a) the PC step finds the relevant drivers, or "parents", of each variable via an iterative independence testing, and (b) the MCI step removes spurious or common parents by conditioning the partial correlations between parents and variables on the parents of the parents.

Start with a set X of n variables that are timeseries of anomalies. The PC algorithm first calculates the correlation between the ith variable in X and the rest of the variables in X at time lag τ. The significant correlations with the ith variable form a set of potential parents X_i^0 at time lag τ, which is ordered by strength of correlation. Then, it calculates the partial correlation between the ith variable and each potential parent in X_i^0, but with a condition that the first variable in X_i^0 has the strongest correlation with the ith variable, testing if the relationship/correlation is mediated by a common variable. If a, b, and c are variables in X, the partial correlation between a and b conditioned on c is calculated by performing a linear regression of a on c and b on c, then correlating the residuals. Variables a and b are conditionally dependent given c, that is, their correlation cannot be explained by the influence of c (not spurious link) if the resulting partial correlation is significant at threshold α. This may reduce the set of parents for the next iteration X_i^1. The process is repeated for this set of parents but with now two conditions, leading to a next (possibly reduced) set of parents X_i^2. When the number of parents is equal to or greater than the number of conditions needed to calculate partial correlation, the algorithm converges.

The MCI step calculates the partial correlation between each variable and its parents at different time lags conditioned on both the set of parents of a and b and the parents of the parents of a and b, essentially removing common driver effects and reducing to a final set of causal parents.

The CEN calculates these causal relationships by performing a standardized multiple regression of each variable with its parents. The final link is represented as the change in standard deviation (σ) of variable at time t if the parent was raised to 1σ at time $t - \tau$. More detail of this algorithm and its comparison to other causality methods can be found in Runge et al. (2019). The PC-MCI algorithm is freely available (Runge, 2022); Tigramite version 4.2 was used for the analysis in this study.

There are many assumptions to using the CEN, including that causal links are determined *relative to the chosen set of variables*. Removing or adding variables may change the CEN, and therefore, it is important for the user to understand the physical system. Other assumptions include the stationarity of relationships and near-linear interactions.

In this study, the CEN visualizes the causal links with a time lag of 1 week. Contemporaneous links are also visualized with no causality direction inferred. The winter season is masked, which means that timescales of variables are restricted to MJJAS season, but the parent (and conditional) timeseries may include data outside the MJJAS season. We set $\alpha = 0.05$, which is the significance threshold as explained above, and a false discovery rate is applied to rectify inflated p-values that result from multiple significance testing (Benjamini & Hochberg, 1995; Benjamini & Yekutieli, 2001). We also set $\tau_{max} = 3$ weeks, which is maximum time delay, though we find that the results are not sensitive to the choice of τ_{max} between 2 and 5.

2.4. Causal Maps

Finally, we experiment with causal maps, which plots the link coefficient from the CEN spatially (Di Capua et al., 2020b). Two one-dimensional timeseries are chosen that have a theoretical relationship with a three-dimensional field. The CEN determines the causal link between one of the one-dimensional timeseries and a timeseries of a grid point from the three-dimensional field, conditioned on the other one-dimensional timeseries. To distinguish between the WNPM- and EAM-forced patterns, as well as the EAM- and EAM-L-forced patterns, we use the weekly WNPM, EAM, and EAM-L timeseries, and the three-dimensional fields of interest are weekly Z200, V850, and OLR. Time lags of 1 and 2 weeks are explored, but, because the 2-week lagged patterns lack statistical significance over CONUS, only the 1-week lagged patterns are presented here.

3. Results

3.1. Link Between BSISO and Great Plains Rainfall

Before constructing the CEN, we first establish the potential influence of subseasonal monsoon variability on CONUS hydroclimate. Composites of OLR and U200 anomalies for the combined BSISO phases (phases 8 + 1, 2 + 3, 4 + 5, and 6 + 7) are depicted in Figure 1, highlighting the northeastward propagation of the regions of active and inactive convection as well as its influence on jet stream anomalies over the North Pacific. In particular, phases 2 + 3 are associated with active convection (negative OLR) over the equatorial Indian Ocean and weak wet anomalies over the EAM region, which corresponds with strengthening or northward displacement of the jet stream over East Asia at 55°N (Figure 1b). During phases 4 + 5, active convection over East Asia strengthens slightly and the positive U200 anomalies are extended over the North Pacific (Figure 1c). Composites of phases 6 + 7 and 8 + 1 present opposite patterns to 2 + 3 and 4 + 5, respectively.

The location of above-normal convection in the ASM region, indicated by BSISO phase, is related to the anomalous probability of Great Plains rainfall events, Great Plains LLJ events, and height patterns over the northeastern Pacific-western North America regions (Figure 2). Above- and below-normal events are defined by upper and lower tercile thresholds, so anomalous probability is defined by the probability deviation from 33%. There is a increased (decreased) probability of a below-normal (above-normal) rainfall event ∼3 weeks after BSISO phase 3 (Figures 2a and 2b). The anomalous probabilities for the rainfall events coincide with the expected anomalous probabilities for the Great Plains LLJ and PNA events (calculated by its standard definition here, as described by CPC; Figures 2b–2f). For example, days with increased probability for the below-normal rainfall event are generally days with an increased probability for strong Great Plains LLJ event and PNA + pattern. This is also true for the above-normal Great Plains rainfall events. Overall, there is an inferred propagation of the signal from the BSISO on these timescales, as seen by the diagonal stripes of increased or decreased anomalous probability, though there are times when this signal is reduced or lacks statistical significance for certain events, lags, and/or phases.

This is further analyzed by investigating the lagged spatial correlation between Great Plains rainfall at $T = 0$ and the OLR, V850, and Z200 anomaly fields at 0, 10, and 20 days before. The correlation between the Great Plains precipitation index and OLR anomalies at $T = 0$ demonstrates the active convection, and hence the precipitation, over the northern Plains (Figure 3a). This corresponds with the strong anomalous southerly flow over the region (Figure 3d) and anomalous low pressure over western North America (Figure 3g). Over the monsoon region and North Pacific, there is a negative correlation with OLR anomalies at 30°N between 90°E and 150°E (Figure 3a, magenta domain) in addition to a positive correlation with EAM-related southerly flow (Figure 3e, black contour outline). A wave train is correlated with the Great Plains precipitation, including our PNA-HL pattern and NPac-L feature (Figure 3g, orange boxes). The PNA-HL pattern has been identified before as an important precursor for

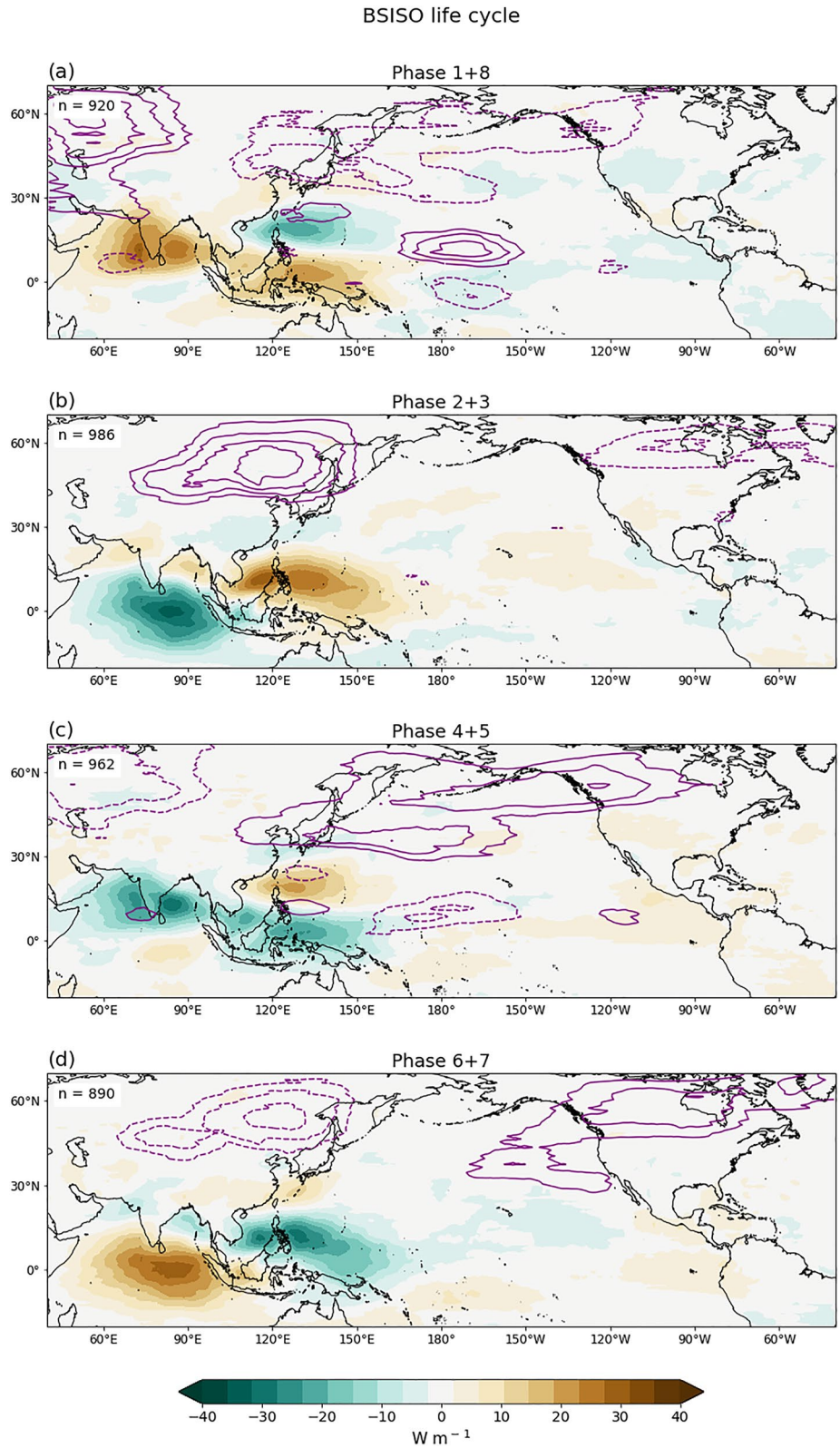

Figure 1. Composited anomalies of Outgoing Longwave Radiation (shaded) and U200 (purple contours) anomalies for boreal summer intraseasonal oscillation (BSISO) combined phases (a) 8 + 1, (b) 2 + 3, (c) 4 + 5, and (d) 6 + 7. U200 anomalies are contoured every 1 m s^{-1} between −5 and 5 m s^{-1}.

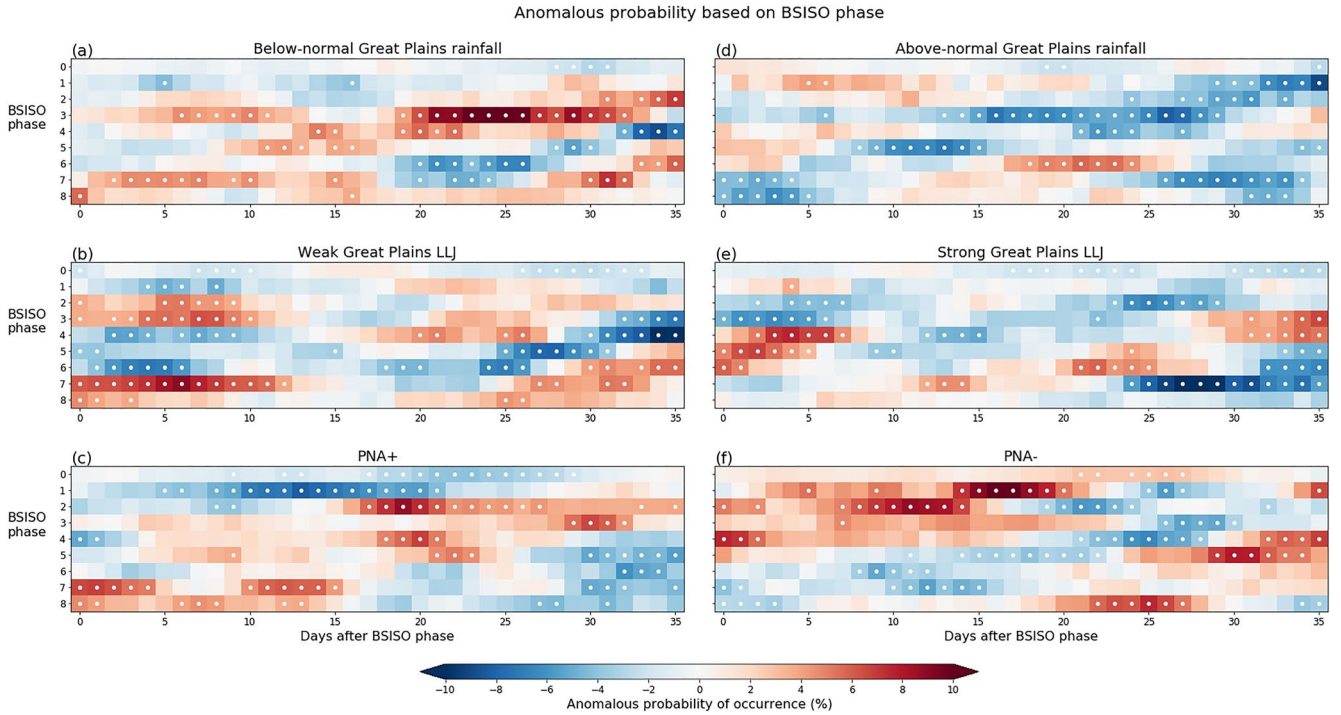

Figure 2. Anomalous probability of the following events for days after a boreal summer intraseasonal oscillation (BSISO) phase: (a) below-normal Great Plains rainfall, (b) weak Great Plains LLJ, (c) PNA + pattern, (d) above-normal Great Plains rainfall, (e) strong Great Plains LLJ, and (f) PNA-pattern. White dots denote statistical significance at the 90% confidence level determined by bootstrapping method with 1,000 iterations.

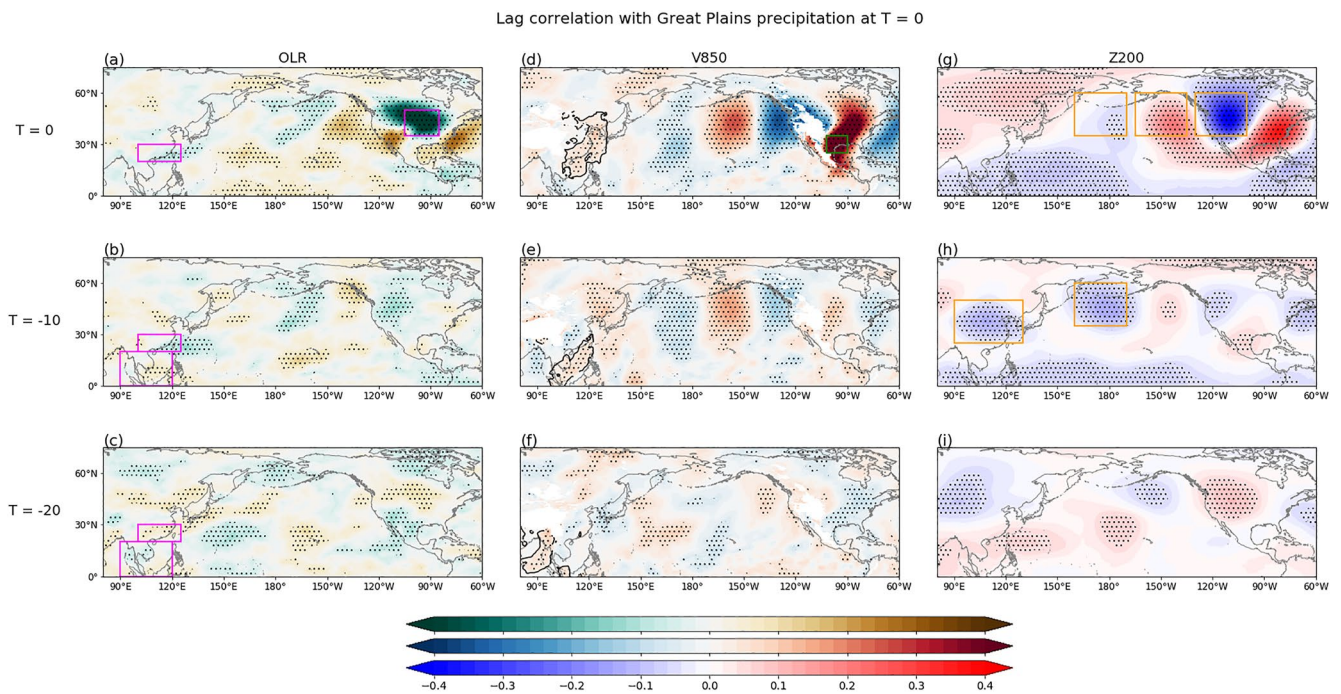

Figure 3. Lag correlation between Great Plains precipitation index at $T = 0$ and (a–c) Outgoing Longwave Radiation (OLR) anomalies at $T = 0$, −10, and −20 days, (d–f) V850 anomalies at $T = 0$, −10, and −20 days, and (g–i) Z200 anomalies at $T = 0$, −10, and −20 days. Pink domains indicate the Great Plains precipitation, East Asian Monsoon (EAM) rainfall, and West North Pacific Monsoon rainfall indices. Green domain indicates the Great Plains LLJ index, and black contour outline highlight the southerly flow over the relevant BSISO region. Orange domains indicate the EAM-L, NPac-L, and PNA-HL indices. Stippling indicates statistical significance at the 90% confidence level and a correlation value >0.05 or <−0.05. See Table 1 for more information about indices.

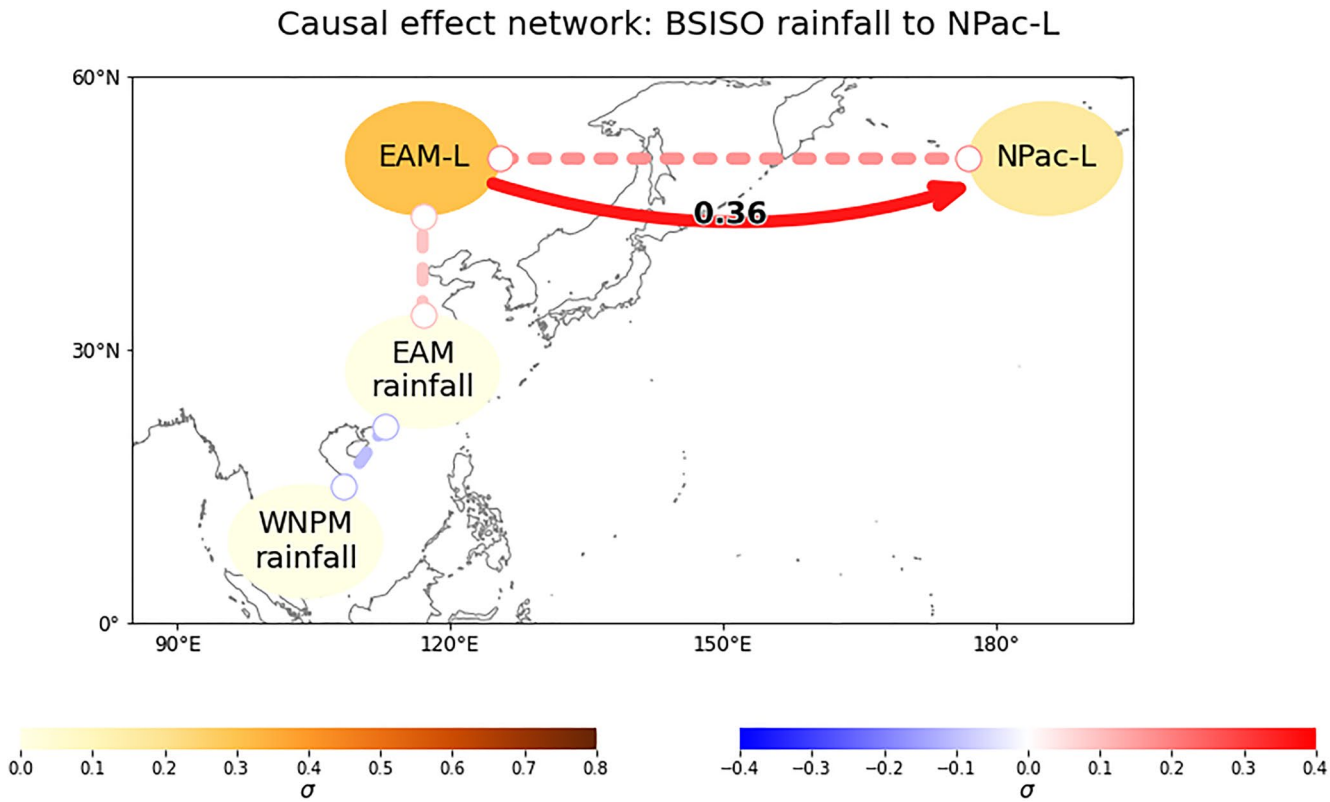

Figure 4. Causal effect network between West North Pacific Monsoon (WNPM) rainfall, East Asian Monsoon (EAM) rainfall, EAM-L, and NPac-L. Color of individual nodes indicates autocorrelated σ change from 1 week to the next. Color of lines or arrows indicate the σ change. Arrows indicate the direction of causality, with strength of σ change annotated on arrow, with lag of 1 week. Dashed lines are contemporaneous links, which, by themselves, do not imply causality.

Plains rainfall events (Harding & Snyder, 2015; Mallakpour & Villarini, 2016; Malloy & Kirtman, 2020; Nayak & Villarini, 2017; Patricola et al., 2015; Rogers & Coleman, 2003).

The correlation between the Great Plains precipitation index and these field anomalies at $T = -10$ (10 days before) reveals that some of the variability of Great Plains rainfall can be due to this cross-Pacific wave train that can be forced/modulated by EAM rainfall (Figures 3b, 3e, and 3h). The correlation with negative OLR and positive V850 anomalies over the EAM region is −0.1 to −0.2, and the wave train pattern is present, including a ∼0.2 correlation with the EAM-L and NPac-L features (Figure 3h, left and right orange domains, respectively). There is also a correlation with positive OLR over the WNPM region 10 days before Great Plains precipitation events, showing an OLR pattern similar to that of combined phases 8 + 1 of the BSISO (cf. Figure 1a). In general, the correlations at $T = -20$ are somewhat opposite to $T = 0$ and $T = -10$, respectively.

These results suggest that the BSISO influences Great Plains rainfall on subseasonal timescales via a cross-Pacific Rossby wave train. We are motivated to test these linkages with a causal discovery algorithm and to confirm if the pathway from EAM rainfall to Great Plains rainfall exists and is considered causal. This method will also approximate the timeframe on which the BSISO-related rainfall anomalies lead to Great Plains anomalies (e.g., within ∼2 weeks, cf. Figure 3).

3.2. CEN for Great Plains Rainfall

Because of the relatively large number of potential drivers, we simplify the discussion of the causal network by separating it into three spatial domains: over East Asia and western North Pacific, over the mid-latitude North Pacific, and over central-eastern North Pacific and North America. In addition, we have input weekly averaged data into the CEN (unlike analysis of the filtered daily data in previous section). First, we test for a causal pathway between the WNPM rainfall, EAM rainfall, EAM-L feature, and NPac-L feature (Figure 4). There is a contemporaneous negative link between weekly averaged WNPM rainfall and EAM rainfall, and a positive

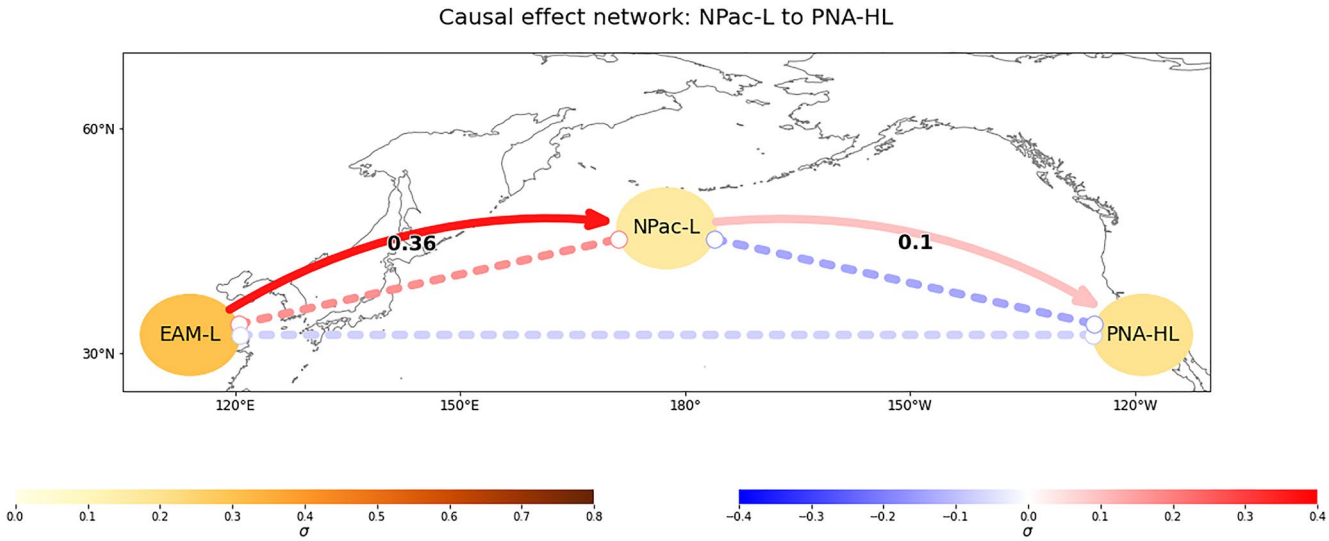

Figure 5. Same as Figure 4, but for the causal effect network between EAM-L, NPac-L, and PNA-HL.

contemporaneous link between weekly averaged EAM rainfall and the EAM-L feature. A strengthening of the weekly averaged EAM-L by 1σ leads to a 0.38σ strengthening in the NPac-L feature the following week. The EAM-L and NPac-L features also have a contemporaneous link. This CEN indicates that the excitation of the Rossby wave activity over the North Pacific often depends on the presence of the EAM-L feature.

Next, we consider the pathway between the different geopotential height features over the North Pacific (Figure 5). A strengthening of the NPac-L by 1σ leads to a 0.1σ strengthening in the PNA-HL pattern the following week, suggesting that the full cross-Pacific Rossby wave train pathway may take up to 2 weeks. The contemporaneous links between these features demonstrate the eastward propagation of the North Pacific wave pattern. For example, the contemporaneous negative link between the EAM-L and PNA-HL is also found in Figure 3i: by the time the Rossby wave reaches North America, the geopotential heights over EAM region are reversed.

Finally, the pathway between NPac-L and the Great Plains LLJ and Great Plains rainfall are visualized in the CEN (Figure 6). A strengthening of the PNA-HL by 1σ leads to a 0.16σ increase in the Great Plains rainfall and 0.09σ strengthening of the Great Plains LLJ the following week. However, a strengthening of the NPac-L by 1σ leads to a 0.2σ increase in the Great Plains rainfall and 0.14σ strengthening of the Great Plains LLJ the following week, which are greater causal links. Considering the contemporaneous link between PNA-HL and Great Plains rainfall and the PNA-HL and Great Plains LLJ are strongly positive, it is likely that the PNA-HL influence on these indices operates on sub-weekly timescales, that is, the weekly averaged data is not resolving the links as causal. However, this demonstrates that the NPac-L may assist in longer-lead prediction of the Great Plains LLJ and rainfall.

The CEN captured the intricacies of the relationships between these indices and their influence on the Great Plains LLJ and Great Plains rainfall. In addition, it demonstrated that the rainfall over the BSISO region is linked to an EAM-L feature that can generate a wave train response over the North Pacific that influences rainfall anomalies over the Great Plains. This can occur on a ∼2-week timescale, potentially advantageous for understanding prediction on the subseasonal timescale.

Because of the contemporaneous relationship between the WNPM rainfall, EAM rainfall, and the EAM-L, it is difficult to assess the true causality between these features and downstream impacts. This motivates the use of causal maps to separate the patterns between WNPM and EAM rainfall as well as between EAM rainfall and EAM-L.

3.3. Causal Maps

By comparing the causal maps for Z200, V850, and OLR (Figures 7–9) with the lag correlation patterns from Figure 3, it is evident that EAM rainfall variability contributes to Great Plains rainfall variability on weekly

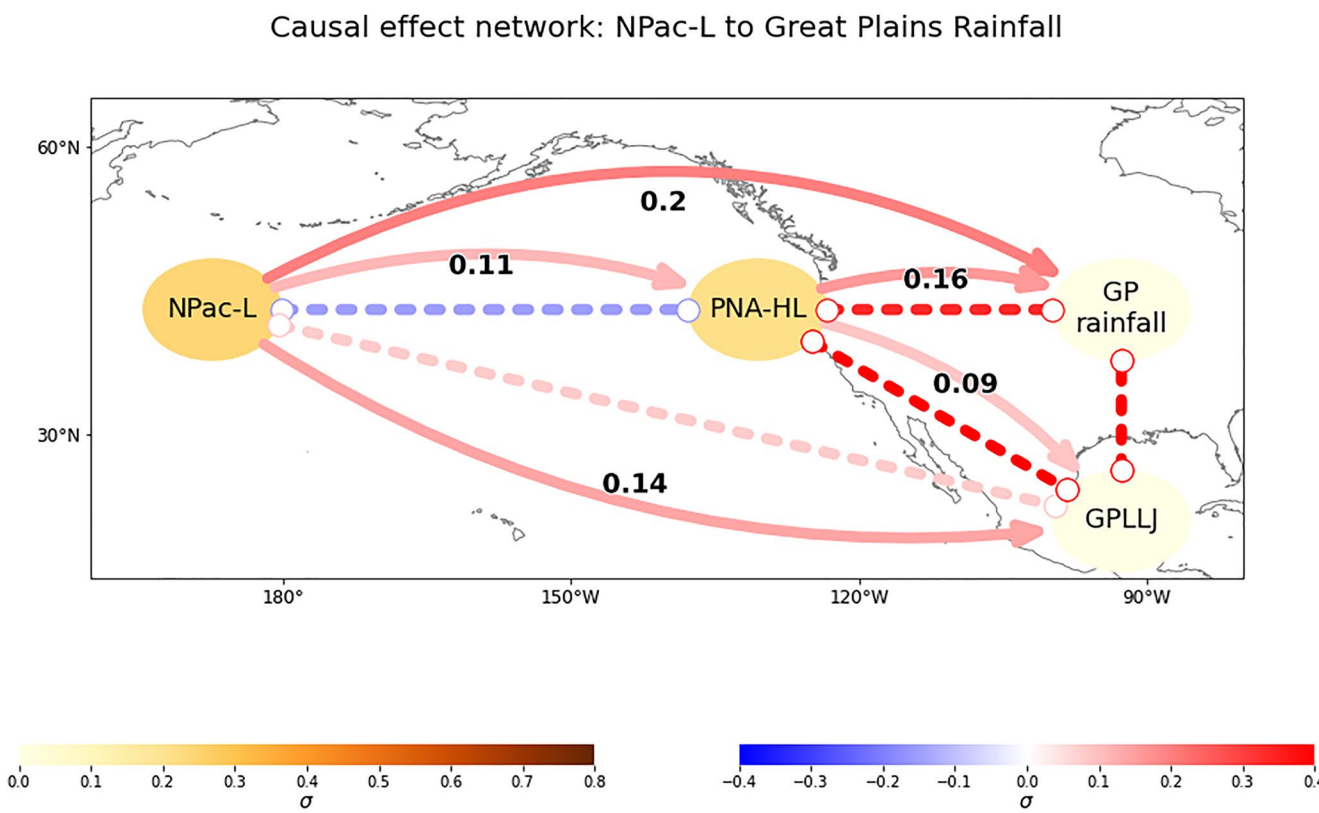

Figure 6. Same as Figure 4, but for the causal effect network between NPac-L, PNA-HL, Great Plains LLJ, and Great Plains rainfall.

timescales. First, we consider the causal linkages between the WNPM rainfall, EAM rainfall, and EAM-L feature at $T = -1$ (one week before) and the Z200 field at $T = 0$. After removing the signal from EAM rainfall, WNPM rainfall affects the Z200 field mostly in the tropics and subtropics, with a 1σ increase in WNPM rainfall causally linked to $\sim 0.2\sigma$ anomalous ridging across the central-eastern tropical Pacific (Figure 7a). After removing the signal from the WNPM, EAM rainfall affects the mid-latitude Z200 field, with a 1σ increase in EAM rainfall

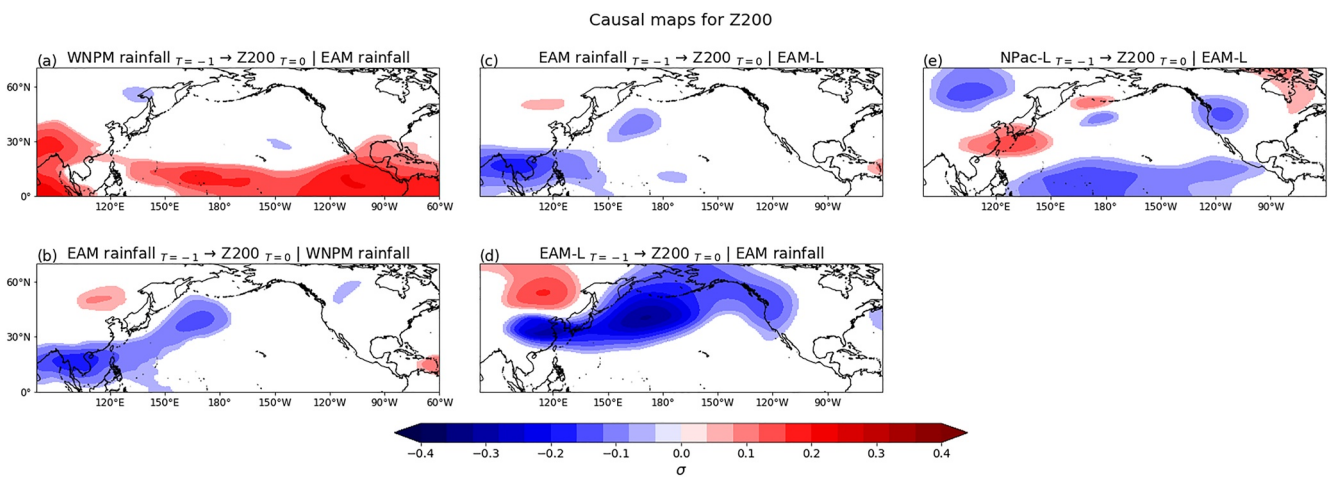

Figure 7. Causal maps showing the causal link value between (a) West North Pacific Monsoon (WNPM) rainfall at $T = -1$ (1 week before) and Z200 at every grid point, with East Asian Monsoon (EAM) rainfall conditioned out, (b) EAM rainfall at $T = -1$ and Z200 at every grid point, with WNPM rainfall conditioned out, (c) EAM rainfall at $T = -1$ and Z200 at every grid point, with EAM-L conditioned out, (d) EAM-L at $T = -1$ and Z200 at every grid point, with EAM rainfall conditioned out, and (e) NPac-L at $T = -1$ and Z200 at every grid point, with EAM-L conditioned out. Causal link value is interpreted the same as arrows in Figures 4–6. Only values with significance at 95% confidence level and a magnitude >0.05 are shown.

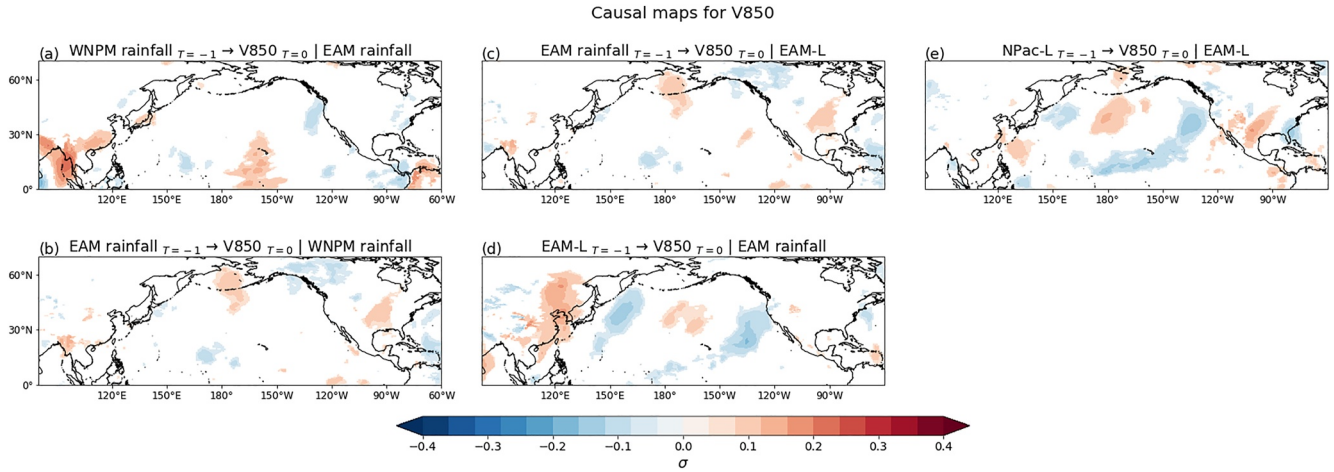

Figure 8. Same as Figure 7, but for links with V850 at every grid point.

causally linked to a ∼0.15–0.2σ anomalous troughing over the WNPM region and North Pacific as well as ∼0.15σ anomalous ridging at higher latitudes in East Asia (Figure 7b). This pattern is similar to the EAM rainfall causal map with the EAM-L signal removed (Figure 7c), but the removal of the EAM-L feature reduces the magnitude of the links. Finally, after removing the signal from EAM rainfall, the EAM-L impact on the Z200 field is prominent, with a 1σ strengthening of the EAM-L causally linked to ∼0.2 anomalous ridging over high-latitude East Asia and 0.3–0.4σ anomalous troughing over the mid-latitude Pacific—including the NPac-L feature—and the Pacific Northwest (Figure 7d). The map of causal links between the EAM rainfall and the Z200 field help explain the Z200 patterns at $T = 0$, and perhaps $T = -10$, from the lag correlations (cf. Figures 3g and 3h) over the EAM region and North Pacific. The strong wave train over North America is not present in the causal maps from the WNPM rainfall, EAM rainfall, or EAM-L. This could mean that the wave train is not explained causally by the WNPM, EAM, or EAM-L, but rather is forced locally, perhaps by feedbacks from Great Plains rainfall. Another possibility is that the causal maps are just not capturing this Z200 wave signal. Nevertheless, EAM rainfall can generate the upstream Rossby wave activity that affects this region. Finally, we consider the next stage of the causal pathway and Rossby wave train. After removing the EAM-L signal (though keeping EAM influence), the NPac-L feature is causally linked to anomalous troughing over the Pacific Northwest U.S. region and tropical Pacific (Figure 7e) 1 week later, demonstrating that the NPac-L feature can strengthen the EAM signals over North America.

Next, we consider causal linkages with the V850 field. WNPM impacts to V850 are most evident in the WNPM and EAM regions as well as the central tropical Pacific (Figure 8a). After removing either the WNPM or EAM-L signal, the causal linkages between EAM rainfall and V850 field are relevant to North America, with a 1σ increase in EAM rainfall leading to a ∼0.15σ strengthening of the Great Plains LLJ (Figures 8b and 8c). EAM rainfall also impacts flow over the high-latitude Bering Sea/Alaska region. The causal linkages between the EAM-L and V850 field are prevalent over the EAM region and North Pacific. In particular, a 1σ strengthening in the EAM-L is causally linked to a 0.1–0.2σ strengthening of the low-level EAM flow. Once again, the EAM rainfall causal links explain more of the lag correlation patterns over North America (cf. Figures 3d and 3e), though the EAM-L is likely playing a role in amplifying the EAM or its signals. Similar to the Z200 causal maps, the NPac-L feature strengthens the EAM-related V850 signals over North America (Figure 8e).

The causal maps for the OLR field further demonstrate the influence of EAM rainfall. While WNPM rainfall impacts to OLR are mostly constrained to the subtropics and tropics (Figure 9a), the EAM rainfall links to OLR are most evident over the North Pacific and North America (Figure 9b). A 1σ increase in EAM rainfall is causally linked to a 0.1–0.2σ decrease in OLR (active convection) over the Great Plains. Patterns and link magnitudes are similar for the EAM rainfall impacts with the EAM-L signal removed (Figure 9c). Interestingly, the EAM-L is causally linked to OLR over the EAM region and Pacific Northwest (Figure 9d). A 1σ strengthening of the EAM-L may lead to a 0.1–0.2σ increase in EAM rainfall in addition to 0.1–0.2σ increase in Pacific Northwest rainfall. These OLR patterns agree with the Z200 patterns from the EAM-L forcing (cf. Figure 7d), that is, active

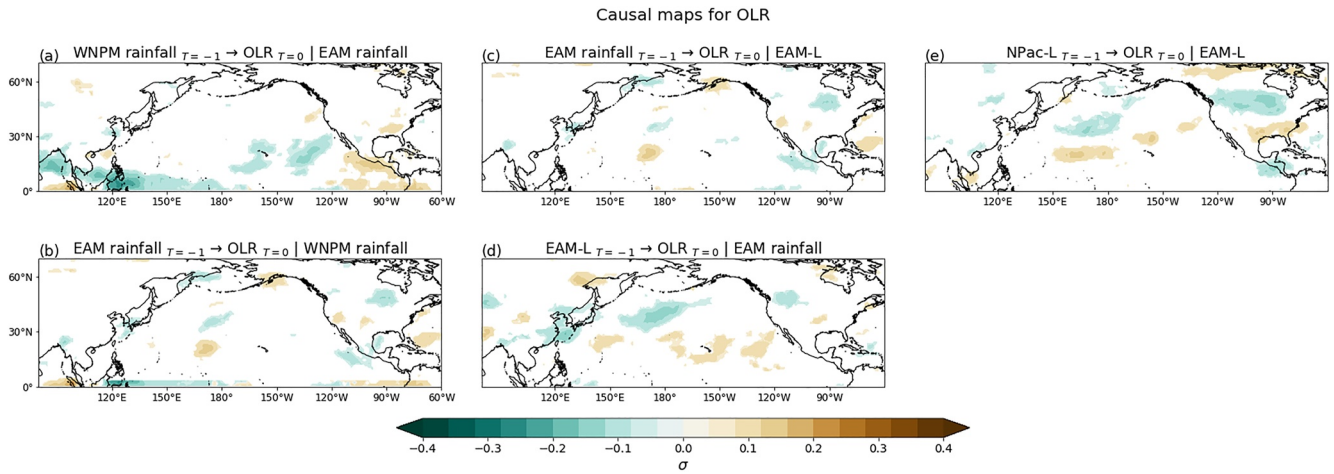

Figure 9. Same as Figure 7, but for links with Outgoing Longwave Radiation (OLR) at every grid point.

convection is expected in these regions with that upper-level geopotential height pattern. The map of causal links from the EAM rainfall is helpful to explain the OLR patterns over the Great Plains region from the $T = 0$ lag correlations (cf. Figure 3a), whereas the map of causal links from the EAM-L feature is helpful for describing the OLR patterns over North Pacific and Pacific Northwest at $T = -10$ days (cf. Figure 3b). By including the NPac-L patterns, there is a clearer OLR signal over North America (Figure 9e). The causal maps indicate that the EAM rainfall often leads to a mid-latitude response over East Asia about 1 week later, including a strengthening of the NPac-L feature. Once the NPac-L feature strengthens, the circulation and OLR anomalies over North America often respond to strengthen the EAM-related signals another 1 week later.

In brief, EAM rainfall and EAM-L feature contribute to Z200 and OLR patterns over the mid-latitude Pacific and/or North America with a 1 week lag. However, EAM rainfall is more directly linked to Great Plains rainfall variability on this timescale, while EAM-L may modulate or amplify EAM-forced activity (or vice versa). Strong upper-level circulation anomalies over North America from Figure 3i were not explained by the monsoons nor the EAM-L feature, suggesting that localized feedbacks by the Great Plains rainfall itself might be forcing or amplifying that pattern.

3.4. Associated Dynamical Mechanisms

To further interpret the causal maps and contextualize these results with respect to potential dynamical mechanisms, we consider the composited 200 hPa anomalies of zonal wind, divergence, stream function as well as horizontal wave activity flux during upper tercile WNPM or EAM days, which we calculated using the daily data. We hypothesize that the magnitude and/or location of the diabatic heating from EAM generates a greater response via jet stream perturbations and Rossby wave activity with greater magnitude than from the WNPM heating, explaining the greater mid-latitude response and resulting teleconnection from EAM rainfall (cf. Figures 7–9).

Strong WNPM days are associated with weak zonal wind anomalies (shaded) over East Asia (Figure 10a). In contrast, for EAM days, there are relatively strong zonal wind anomalies close to the climatological East Asian jet stream (black contours) collocated with EAM-related divergence (purple contours; Figure 10b). The WNPM and EAM days are associated with a similar pattern of stream function anomalies over Eurasia (shaded anomalies in Figures 10c and 10d), resembling the CGT, which has been found to influence North American summer climate (Beverley et al., 2021; Di Capua et al., 2020b; Ding & Wang, 2005). However, there is a regional amplification of the CGT over East Asia and West North Pacific only during EAM days (Figure 10d). Wave activity flux is used to diagnose the wave energy propagation in a zonally varying basic flow (calculated as MJJAS mean state here) due to stationary Rossby waves (Takaya & Nakamura, 1997, 2001). The wave activity flux is similar for both WNPM and EAM, that often Rossby waves will move equatorward over the North Pacific (northerly arrows over West North Pacific). However, there is another pathway in which Rossby wave activity moves eastward over North America. The amplified anomalous stream function pattern over East Asia and cross-Pacific wave pattern during the EAM days suggests that the EAM forcing can more effectively trigger or modulate Rossby waves that

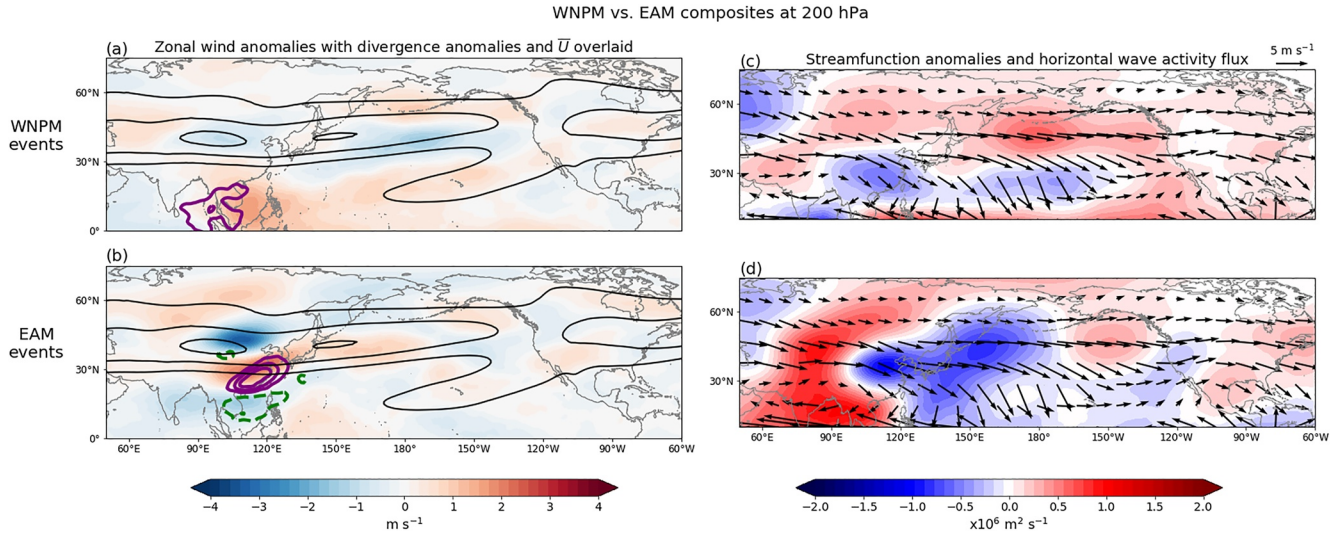

Figure 10. 200 hPa zonal wind anomalies (shaded), with 200 hPa divergence anomalies (purple/green contours) and $\overline{U}$ (black contours) overlaid, for (a) upper tercile West North Pacific Monsoon (WNPM) days and (b) upper tercile East Asian Monsoon (EAM) days. 200 hPa stream function anomalies and horizontal wave activity flux for (a) upper tercile WNPM days and (b) upper tercile EAM days. Divergence anomalies are contoured every 1×10^{-6} s^{-1} between -3 and -1 $^{-6}$ s^{-1} (green dashed) as well as 1 and 3×10^{-6} s^{-1} (purple solid), and $\overline{U}$ is contoured every 10 m s^{-1} between 10 and 30 m s^{-1}. Arrow scale for wave activity flux is on upper right corner of (c).

propagate to North America. Overall, the Z200 response from the lagged correlation analysis (cf. Figure 3g) and causal maps (cf. Figures 7b and 7c) can be explained by this teleconnection excitation from EAM-related divergence, likely due to release of diabatic heating.

4. Summary and Discussion

Here, we explored the subseasonal predictability of Great Plains rainfall with a theory-guided application of CENs. Using a traditional lead-lag analysis approach, we found that the BSISO is related to Great Plains rainfall, the Great Plains LLJ, and PNA-HL pattern via a cross-Pacific wave train. The time between EAM-L anomalies potentially influencing Great Plains rainfall anomalies is ∼2 weeks; therefore, BSISO forcing or modulation of the EAM-L may be valuable forecast of opportunity for subseasonal prediction of Great Plains rainfall. Causal link patterns and associated RWS anomalies from the EAM rainfall revealed that the EAM is causally linked to excitation or modulation of Rossby wave patterns, leading to downstream Great Plains LLJ and rainfall anomalies. Anomalous geopotential height activity over EAM region (e.g., EAM-L pattern) may have a role in modulating the EAM-related patterns.

We applied similar techniques to Di Capua et al. (2020a) and Di Capua et al. (2020b) to understand subseasonal North American hydroclimate variability, and we focus on the EAM as a regionally significant branch of the ASM based on results from Malloy and Kirtman (2022). The subseasonal patterns related to WNPM and EAM convection in Figure 3 are different from the seasonal EAM-forced patterns from Malloy and Kirtman (2022), demonstrating the importance of timescale for quantifying impacts (Yang et al., 2020). In addition, the definition/index and spatial scale of the drivers may affect interpretation of results; for instance, the WNPM in Di Capua et al. (2020b) was defined by maximum covariance analysis (MCA) between tropical OLR and mid-latitude upper-level heights, highlighting their different approach in defining this region of active convection and its remote impacts. It raises the question of whether the definition of the WNPM via MCA methodology in Di Capua et al. (2020b) is too broad to capture the true source of the teleconnection since it conflates both the effects of the WNPM and EAM rainfall, or whether the definition of the local-scale rainfall in this study is weakening the teleconnection signals downstream. Nevertheless, our causal map results generally agree with the patterns from their study, though future analysis should consider the (dis)advantages of both approaches.

There are limitations to using the CEN, such as the causal links are only determined based on the set of drivers here. Adding other known influences of Great Plains rainfall, such as the North Atlantic subtropical high (L. Li

et al., 2012; W. Li et al., 2011; Nieto Ferreira & Rickenbach, 2020; Wei et al., 2019), may change the CEN. In addition, despite the ease of using weekly averaged indices for the CEN, there are drawbacks. Linkages considered contemporaneous on this weekly timescale may actually be causal on a sub-weekly timescale. For instance, the contemporaneous link between EAM rainfall and EAM-L (Figure 4) and the contemporaneous link between the Great Plains LLJ and rainfall (Figure 6) may be considered causal on daily timescales. Several modifications could be made to this study's CEN, such as inputting the RWS or north-south temperature gradient over the EAM region as a driver. Though we have not explored all possible input drivers to the CEN, we have demonstrated how the CEN can be used to gain a deeper understanding compared to simple correlation or regression analyses, aiming to separate correlation and causation between events or features. Future work should also consider potential nonlinear relationships between these drivers, perhaps through performing nonlinear independence testing.

Interestingly, the EAM-L feature was important for modulating Rossby wave activity over the North Pacific, even when removing the influence of EAM. This suggests that the EAM-L feature can be forced by non-EAM activity. The EAM is only a regional branch of the ASM system. Other sub-monsoonal systems via the CGT might be impacting the variability of geopotential height activity over the EAM region (Di Capua et al., 2020a; Ding & Wang, 2005; Ding et al., 2011; Kornhuber et al., 2019; Zhao et al., 2018; F. Zhou et al., 2020), and on different timescales, which should be explored further. F. Zhou et al. (2020) suggested that the EAM might maintain the CGT through latent heat release, which is supported in our causal map results as well as our EAM composite of 200 hPa stream function anomalies and wave activity flux (cf. Figure 10d). In addition, other aspects of subseasonal variability unrelated to the monsoon might be involved. For example, the NAO has been shown to modulate upper-level circulation over Eurasia (Di Capua et al., 2020a; Syed et al., 2012; Wang et al., 2018). Finally, the amplified wave pattern in Figure 3g was not produced in our causal maps, which suggests that perhaps local mechanisms (e.g., land-atmosphere or precipitation feedback processes) are involved (Dirmeyer et al., 2003; Guo et al., 2011; Jong et al., 2021; Koster et al., 2004, 2006).

Future work should address the subseasonal predictability of summer Great Plains rainfall via the BSISO or, more generally, wave activity over the EAM region, in climate forecast models. The CEN and causal maps with model data may reveal dissimilar casual linkages from observations, which would be valuable for understanding model biases of these teleconnections. Additionally, noting the influence of El Niño-Southern Oscillation on monsoon variability (Ding et al., 2011; F. Liu et al., 2016; Malloy & Kirtman, 2020) and general summertime predictability over CONUS (Krishnamurthy et al., 2021; J. Y. Lee et al., 2011; Y. Liu et al., 2019; F. Zhou et al., 2020), it would be advantageous to investigate the potential impacts warm or cool phases have on the causal pathways and link magnitudes. It is possible that tropical forcing might influence the predictability of these casual links, such that EAM-forced patterns might be stronger during El Nino years (Malloy & Kirtman, 2022) or ENSO might have a greater causal link to the PNA, Great Plains LLJ, and related Plains rainfall.

Data Availability Statement

All data in this study is available online. ERA5 data can be accessed through their website https://www.ecmwf.int/en/forecasts/datasets/reanalysis-datasets/era5 (Hersbach et al., 2020). The CPC Global Unified Gauge-based Analysis data was provided by the NOAA PSL, Boulder, Colorado, USA, from their website at https://psl.noaa.gov (Chen et al., 2008; Xie et al., 2007). OLR data was taken from the National Oceanic and Atmospheric Administration (NOAA) Climate Data Record from https://www.ncei.noaa.gov/access/metadata/landing-page/bin/iso?id=gov.noaa.ncdc:C00875 (H.-T. Lee & Program, 2011).
The PC-MCI algorithm (Runge, 2022) is publicly available and can be found at the https://doi.org/10.5281/zenodo.6247837 or by visiting https://doi.org/10.5281/zenodo.6247837.

Acknowledgments
The authors would like to acknowledge that this work was supported through NOAA Grants NA15OAR4320064, NA16OAR4310141, N16OAR4310149, and NA20OAR430472 and DOE Grant DE-SC0019433. BPK is the William R Middelthon Chair of Earth Sciences and is grateful for the assoicated support. The authors would also like to thank three anonymous reviewers for their thoughtful feedback, which greatly improved the paper.

References

Agrawal, S., Ferguson, C. R., Bosart, L., & Burrows, D. A. (2021). Teleconnections governing the interannual variability of Great Plains low-level jets in May. *Journal of Climate*, *34*(12), 4785–4802. https://doi.org/10.1175/jcli-d-20-0451.1

Algarra, I., Eiras-Barca, J., Miguez-Macho, G., Nieto, R., & Gimeno, L. (2019). On the assessment of the moisture transport by the Great Plains low-level jet. *Earth System Dynamics*, *10*(1), 107–119. https://doi.org/10.5194/esd-10-107-2019

Arcodia, M. C., Kirtman, B. P., & Siqueira, L. S. (2020). How MJO teleconnections and ENSO interference impacts U.S. precipitation. *Journal of Climate*, *33*(11), 4621–4640. https://doi.org/10.1175/jcli-d-19-0448.1

Arritt, R. W., Rink, T. D., Segal, M., Todey, D. P., Clark, C. A., Mitchell, M. J., & Labas, K. M. (1997). The Great Plains low-level jet during the warm season of 1993. *Monthly Weather Review*, *125*(9), 2176–2192. https://doi.org/10.1175/1520-0493(1997)125<2176:tgpllj>2.0.co;2

Benjamini, Y., & Hochberg, Y. (1995). Controlling the false discovery rate: A practical and powerful approach to multiple testing. *Journal of the Royal Statistical Society: Series B*, *57*(1), 289–300. https://doi.org/10.1111/j.2517-6161.1995.tb02031.x

Benjamini, Y., & Yekutieli, D. (2001). The control of the false discovery rate in multiple testing under dependency. *Annals of Statistics*, 1165–1188.

Beverley, J. D., Woolnough, S. J., Baker, L. H., Johnson, S. J., Weisheimer, A., & O'Reilly, C. H. (2021). Dynamical mechanisms linking Indian monsoon precipitation and the circumglobal teleconnection. *Climate Dynamics*, *57*(9–10), 2615–2636. https://doi.org/10.1007/s00382-021-05825-6

Chen, M., Shi, W., Xie, P., Silva, V. B., Kousky, V. E., Higgins, R. W., & Janowiak, J. E. (2008). Assessing objective techniques for gauge-based analyses of global daily precipitation. *Journal of Geophysical Research: Atmospheres*, *113*(D4), D04110. https://doi.org/10.1029/2007JD009132

Cook, K. H., Vizy, E. K., Launer, Z. S., & Patricola, C. M. (2008). Springtime intensification of the Great Plains low-level jet and Midwest precipitation in GCM simulations of the twenty-first century. *Journal of Climate*, *21*(23), 6321–6340. https://doi.org/10.1175/2008JCLI2355.1

Di Capua, G., Kretschmer, M., Donner, R. V., Van Den Hurk, B., Vellore, R., Krishnan, R., & Coumou, D. (2020a). Tropical and mid-latitude teleconnections interacting with the Indian summer monsoon rainfall: A theory-guided causal effect network approach. *Earth System Dynamics*, *11*(1), 17–34. https://doi.org/10.5194/esd-11-17-2020

Di Capua, G., Runge, J., Donner, R. V., van den Hurk, B., Turner, A. G., Vellore, R., et al. (2020b). Dominant patterns of interaction between the tropics and mid-latitudes in boreal summer: Causal relationships and the role of timescales. *Weather and Climate Dynamics*, *1*(2), 519–539. https://doi.org/10.5194/wcd-1-519-2020

Ding, Q., & Wang, B. (2005). Circumglobal teleconnection in the Northern Hemisphere summer. *Journal of Climate*, *18*(17), 3483–3505. https://doi.org/10.1175/jcli3473.1

Ding, Q., Wang, B., Wallace, J. M., & Branstator, G. (2011). Tropical-extratropical teleconnections in boreal summer: Observed interannual variability. *Journal of Climate*, *24*(7), 1878–1896. https://doi.org/10.1175/2011JCLI3621.1

Dirmeyer, P. A., Fennessy, M. J., & Marx, L. (2003). Low skill in dynamical prediction of boreal summer climate: Grounds for looking beyond sea surface temperature. *Journal of Climate*, *16*(6), 995–1002. https://doi.org/10.1175/1520-0442(2003)016<0995:lsidpo>2.0.co;2

Guo, Z., Dirmeyer, P. A., & DelSole, T. (2011). Land surface impacts on subseasonal and seasonal predictability. *Geophysical Research Letters*, *38*(24). https://doi.org/10.1029/2011gl049945

Harding, K., & Snyder, P. (2015). The relationship between the Pacific–North American teleconnection pattern, the Great Plains low-level jet, and north central U.S. heavy rainfall events. *Journal of Climate*, *28*(17), 6729–6742. https://doi.org/10.1175/jcli-d-14-00657.1

Hersbach, H., Bell, B., Berrisford, P., Hirahara, S., Horányi, A., Muñoz-Sabater, J., et al. (2020). The ERA5 global reanalysis. *Quarterly Journal of the Royal Meteorological Society*, *146*(730), 1999–2049. https://doi.org/10.1002/qj.3803

Higgins, R. W., Yao, Y., Yarosh, E. S., Janowiak, J. E., & Mo, K. C. (1997). Influence of the Great Plains low-level jet on summertime precipitation and moisture transport over the central United States. *Journal of Climate*, *10*(3), 481–507. https://doi.org/10.1175/1520-0442(1997)010<0481:iotgpl>2.0.co;2

Jong, B. T., Ting, M., & Seager, R. (2021). Assessing ENSO summer teleconnections, impacts, and predictability in North America. *Journal of Climate*, *34*(9), 3629–3643. https://doi.org/10.1175/JCLI-D-20-0761.1

Kornhuber, K., Osprey, S., Coumou, D., Petri, S., Petoukhov, V., Rahmstorf, S., & Gray, L. (2019). Extreme weather events in early summer 2018 connected by a recurrent hemispheric wave-7 pattern. *Environmental Research Letters*, *14*(5), 054002. https://doi.org/10.1088/1748-9326/ab13bf

Koster, R. D., Dirmeyer, P. A., Guo, Z., Bonan, G., Chan, E., Cox, P., et al. (2004). Regions of strong coupling between soil moisture and precipitation. *Science*, *305*(5687), 1138–1140. https://doi.org/10.1126/science.1100217

Koster, R. D., Sud, Y., Guo, Z., Dirmeyer, P. A., Bonan, G., Oleson, K. W., et al. (2006). Glace: The global land-atmosphere coupling experiment. Part I: Overview. *Journal of Hydrometeorology*, *7*(4), 590–610. https://doi.org/10.1175/jhm510.1

Kretschmer, M., Coumou, D., Donges, J. F., & Runge, J. (2016). Using causal effect networks to analyze different arctic drivers of midlatitude winter circulation. *Journal of Climate*, *29*(11), 4069–4081. https://doi.org/10.1175/jcli-d-15-0654.1

Krishnamurthy, V., Meixner, J., Stefanova, L., Wang, J., Worthen, D., Moorthi, S., et al. (2021). Sources of subseasonal predictability over conus during boreal summer. *Journal of Climate*, *34*(9), 3273–3294. https://doi.org/10.1175/jcli-d-20-0586.1

Lee, H.-T., & NOAA CDR Program (2011). NOAA Climate Data Record (CDR) of daily Outgoing Longwave Radiation (OLR), version 1.2. [Dataset]. National Centers for Environmental Information, NESDIS, NOAA, U.S. Department of Commerce. Retrieved from https://www.ncei.noaa.gov/access/metadata/landing-page/bin/iso?id=gov.noaa.ncdc:C00875

Lee, J. Y., Wang, B., Ding, Q., Ha, K. J., Ahn, J. B., Kumar, A., et al. (2011). How predictable is the Northern Hemisphere summer upper-tropospheric circulation? *Climate Dynamics*, *37*(5–6), 1189–1203. https://doi.org/10.1007/s00382-010-0909-9

Lee, S. S., & Wang, B. (2016). Regional boreal summer intraseasonal oscillation over Indian Ocean and western Pacific: Comparison and predictability study. *Climate Dynamics*, *46*(7–8), 2213–2229. https://doi.org/10.1007/s00382-015-2698-7

Li, L., Li, W., & Kushnir, Y. (2012). Variation of the North Atlantic subtropical high western ridge and its implication to southeastern U.S. summer precipitation. *Climate Dynamics*, *39*(6), 1401–1412. https://doi.org/10.1007/s00382-011-1214-y

Li, W., Li, L., Fu, R., Deng, Y., & Wang, H. (2011). Changes to the North Atlantic subtropical high and its role in the intensification of summer rainfall variability in the southeastern United States. *Journal of Climate*, *24*(5), 1499–1506. https://doi.org/10.1175/2010jcli3829.1

Liu, F., Li, T., Wang, H., Deng, L., & Zhang, Y. (2016). Modulation of boreal summer intraseasonal oscillations over the western North Pacific by ENSO. *Journal of Climate*, *29*(20), 7189–7201. https://doi.org/10.1175/JCLI-D-15-0831.1

Liu, Y., Ke, Z., & Ding, Y. (2019). Predictability of East Asian summer monsoon in seasonal climate forecast models. *International Journal of Climatology*, *39*(15), 5688–5701. https://doi.org/10.1002/joc.6180

Lopez, H., Lee, S. K., Dong, S., Goni, G., Kirtman, B., Atlas, R., & Kumar, A. (2019). East Asian monsoon as a modulator of U.S. Great Plains heat waves. *Journal of Geophysical Research: Atmospheres*, *124*(12), 6342–6358. https://doi.org/10.1029/2018JD030151

Mallakpour, I., & Villarini, G. (2016). Investigating the relationship between the frequency of flooding over the central United States and large-scale climate. *Advances in Water Resources*, *92*, 159–171. https://doi.org/10.1016/j.advwatres.2016.04.008

Malloy, K. M., & Kirtman, B. P. (2020). Predictability of midsummer Great Plains low-level jet and associated precipitation. *Weather and Forecasting*, *35*(1), 215–235. https://doi.org/10.1175/WAF-D-19-0103.1

Malloy, K. M., & Kirtman, B. P. (2022). The summer Asia-North America teleconnection and its modulation by ENSO in community atmosphere model, version 5 (CAM5). *Climate Dynamics*, *59*(7–8), 2213–2230. https://doi.org/10.1007/s00382-022-06205-4

Moon, J. Y., Wang, B., Ha, K. J., & Lee, J. Y. (2013). Teleconnections associated with Northern Hemisphere summer monsoon intraseasonal oscillation. *Climate Dynamics*, *40*(11–12), 2761–2774. https://doi.org/10.1007/s00382-012-1394-0

Nayak, M. A., & Villarini, G. (2017). A long-term perspective of the hydroclimatological impacts of atmospheric rivers over the central United States. *Water Resources Research*, *53*(2), 1144–1166. https://doi.org/10.1002/2016WR019033

Nieto Ferreira, R., & Rickenbach, T. M. (2020). Effects of the North Atlantic subtropical high on summertime precipitation organization in the southeast United States. *International Journal of Climatology*, *40*(14), 5987–6001. https://doi.org/10.1002/joc.6561

Patricola, C. M., Chang, P., & Saravanan, R. (2015). Impact of Atlantic SST and high-frequency atmospheric variability on the 1993 and 2008 Midwest floods: Regional climate model simulations of extreme climate events. *Climatic Change*, *129*(3–4), 397–411. https://doi.org/10.1007/s10584-013-0886-1

Rogers, J. C., & Coleman, J. S. (2003). Interactions between the Atlantic multidecadal oscillation, El Niño/La Niña, and the PNA in winter Mississippi valley stream flow. *Geophysical Research Letters*, *30*(10), 1518. https://doi.org/10.1029/2003gl017216

Runge, J. (2018). Causal network reconstruction from timeseries: From theoretical assumptions to practical estimation. *Chaos: An Interdisciplinary Journal of Nonlinear Science*, *28*(7), 075310. https://doi.org/10.1063/1.5025050

Runge, J. (2020). Discovering contemporaneous and lagged causal relations in autocorrelated nonlinear timeseries data sets. In *Proceedings of the 36th Conference on Uncertainty in Artificial Intelligence (UAI)* (pp. 1388–1397). PMLR.

Runge, J. (2022). jakobrunge/tigramite: Tigramite 5.0. Zenodo. https://doi.org/10.5281/zenodo.6247837

Runge, J., Nowack, P., Kretschmer, M., Flaxman, S., & Sejdinovic, D. (2019). Detecting and quantifying causal associations in large nonlinear timeseries data sets. *Science Advances*, *5*(11), eaau4996. https://doi.org/10.1126/sciadv.aau4996

Runge, J., Petoukhov, V., & Kurths, J. (2014). Quantifying the strength and delay of climatic interactions: The ambiguities of cross correlation and a novel measure based on graphical models. *Journal of Climate*, *27*(2), 720–739. https://doi.org/10.1175/jcli-d-13-00159.1

Spirtes, P., Glymour, C. N., Scheines, R., & Heckerman, D. (2000). *Causation, prediction, and search*. MIT Press.

Syed, F. S., Yoo, J. H., Körnich, H., & Kucharski, F. (2012). Extratropical influences on the interannual variability of south-Asian monsoon. *Climate Dynamics*, *38*(7), 1661–1674. https://doi.org/10.1007/s00382-011-1059-4

Takaya, K., & Nakamura, H. (1997). A formulation of a wave-activity flux for stationary Rossby waves on a zonally varying basic flow. *Geophysical Research Letters*, *24*(23), 2985–2988. https://doi.org/10.1029/97gl03094

Takaya, K., & Nakamura, H. (2001). A formulation of a phase-independent wave-activity flux for stationary and migratory quasi-geostrophic eddies on a zonally varying basic flow. *Journal of the Atmospheric Sciences*, *58*(6), 608–627. https://doi.org/10.1175/1520-0469(2001)058<0608:afoapi>2.0.co;2

Trenberth, K. E., Branstator, G. W., Karoly, D., Kumar, A., Lau, N. C., & Ropelewski, C. (1998). Progress during TOGA in understanding and modeling global teleconnections associated with tropical sea surface temperatures. *Journal of Geophysical Research: Oceans*, *103*(C7), 14291–14324. https://doi.org/10.1029/97jc01444

Wang, Z., Yang, S., Lau, N.-C., & Duan, A. (2018). Teleconnection between summer NAO and East China rainfall variations: A bridge effect of the Tibetan Plateau. *Journal of Climate*, *31*(16), 6433–6444. https://doi.org/10.1175/jcli-d-17-0413.1

Weaver, S. J., & Nigam, S. (2008). Variability of the Great Plains low-level jet: Large-scale circulation context and hydroclimate impacts. *Journal of Climate*, *21*(7), 1532–1551. https://doi.org/10.1175/2007JCLI1586.1

Weaver, S. J., Ruiz-Barradas, A., & Nigam, S. (2009). Pentad evolution of the 1988 drought and 1993 flood over the Great Plains: An NARR perspective on the atmospheric and terrestrial water balance. *Journal of Climate*, *22*(20), 5366–5384. https://doi.org/10.1175/2009JCLI2684.1

Wei, W., Li, W., Deng, Y., & Yang, S. (2019). Intraseasonal variation of the summer rainfall over the southeastern United States. *Climate Dynamics*, *53*(1–2), 1171–1183. https://doi.org/10.1007/s00382-018-4345-6

Xie, P., Yatagai, A., Chen, M., Hayasaka, T., Fukushima, Y., Liu, C., & Yang, S. (2007). A gauge-based analysis of daily precipitation over East Asia. *Journal of Hydrometeorology*, *8*(3), 607–626. https://doi.org/10.1175/JHM583.1

Yang, Y., Zhu, Z., Li, T., & Yao, M. (2020). Effects of western Pacific intraseasonal convection on surface air temperature anomalies over North America. *International Journal of Climatology*, *40*(6), 2913–2923. https://doi.org/10.1002/joc.6373

Yasunari, T. (1979). Cloudiness fluctuations associated with the Northern Hemisphere summer monsoon. *Journal of the Meteorological Society of Japan. Series II*, *57*(3), 227–242. https://doi.org/10.2151/jmsj1965.57.3_227

Yasunari, T. (1980). A quasi-stationary appearance of 30–40 days period in the cloudiness fluctuations during the summer monsoon over India. *Journal of the Meteorological Society of Japan. Series II*, *58*(3), 225–229. https://doi.org/10.2151/jmsj1965.58.3_225

Zhao, S., Deng, Y., & Black, R. X. (2018). An intraseasonal mode of atmospheric variability relevant to the U.S. hydroclimate in boreal summer: Dynamic origin and East Asia connection. *Journal of Climate*, *31*(24), 9855–9868. https://doi.org/10.1175/JCLI-D-18-0206.1

Zhou, F., Ren, H. L., Hu, Z. Z., Liu, M. H., Wu, J., & Liu, C. Z. (2020). Seasonal predictability of primary East Asian summer circulation patterns by three operational climate prediction models. *Quarterly Journal of the Royal Meteorological Society*, *146*(727), 629–646. https://doi.org/10.1002/qj.3697

Zhou, S., L'Heureux, M., Weaver, S., & Kumar, A. (2012). A composite study of the MJO influence on the surface air temperature and precipitation over the continental United States. *Climate Dynamics*, *38*(7–8), 1459–1471. https://doi.org/10.1007/s00382-011-1001-9

Zhu, Z., & Li, T. (2016). A new paradigm for continental U.S. summer rainfall variability: Asia–North America teleconnection. *Journal of Climate*, *29*(20), 7313–7327. https://doi.org/10.1175/JCLI-D-16-0137.1

Zhu, Z., & Li, T. (2018). Amplified contiguous United States summer rainfall variability induced by East Asian monsoon interdecadal change. *Climate Dynamics*, *50*(9–10), 3523–3536. https://doi.org/10.1007/s00382-017-3821-8